Low Temperature Physics/Fizika Nizkikh Temperatur, 2013, v. 39, No. 7, pp. 771–779

Electronic structure, phonon spectra and electron–phonon interaction in ScB_2

S.M. Sichkar[1] and V.N. Antonov[1,2]

[1]*Institute of Metal Physics, 36 Vernadsky Str., 03680 Kiev-142, Ukraine*

[2]*Ames Laboratory, U.S. Department of Energy, Ames, Iowa 50011, USA*

E-mail: antonov@imp.kiev.ua

Received February 11, 2013, revised March 1, 2013

The electronic structure, Fermi surface, angle dependence of the cyclotron masses and extremal cross sections of the Fermi surface, phonon spectra, electron–phonon Eliashberg and transport spectral functions, temperature dependence of electrical resistivity of the ScB_2 diboride were investigated from first principles using the fully relativistic and full potential linear muffin-tin orbital methods. The calculations of the dynamic matrix were carried out within the framework of the linear response theory. A good agreement with experimental data of electron–phonon spectral functions, electrical resistivity, cyclotron masses and extremal cross sections of the Fermi surface was achieved.

PACS: 75.50.Cc Other ferromagnetic metals and alloys;
71.20.Lp Intermetallic compounds;
71.15.Rf Relativistic effects.

Keywords: diborides, superconductivity, Fermi surface.

1. Introduction

The discovery of superconductivity in MgB_2 at 39 K by Akimitsu [1] has lead to booming activity in the physics community and activated a search for superconductivity in other diborides. Natural candidates for this search are AB_2-type light metal diborides (A = Li, Be, Al). However, up to now superconductivity has not been reported in the majority of these compounds [2]. Only very recently superconductivity below 1 K (T_c = 0.72 K) has been reported in $BeB_{2.75}$ [3]. According to Ref. 4 no superconducting transition down to 0.42 K has been observed in powders of diborides of transition metals (M = Ti, Zr, Hf, V, Cr, Mo, U). NbB_2 is expected to superconduct with a rather low transition temperature (< 1 K), and contradictory reports about superconductivity up to T_c = 9.5 K in TaB_2 can be found in Ref. 4. For ScB_2 only low-temperature superconductivity was found with $T_c \sim 1.5$ K [5]. Finally, the reported T_c = 7 K in ZrB_2 encourages further studies of these diborides [2].

Quite a number of theoretical studies of the electronic properties of the diborides are known to date [6–23]. Ivanovskii *et al*. [9] performed full potential linear muffin-tin orbital (FP-LMTO) calculations of all hexagonal diborides of 3*d* (Sc, Ti, ..., Fe), 4*d* (Y, Zr, ..., Ru), and 5*d* (La, Hf, ..., Os) metals and analyzed the variations in their chemical stability and some other properties (e.g., melting temperatures, enthalpies of formation). They found that the evolution of their band structures can be described within a rigid-band model. For M = Ti, Zr, Hf energy Fermi (ε_F) falls near the density of state (DOS) minimum (pseudogap) between the fully occupied bonding bands and unoccupied antibonding bands. Sc, Y, La diborides have partially unoccupied bonding bands. Vajeeston *et al*. [11] investigated the electronic structure and ground state properties of AlB_2 type transition metal diborides MB_2 (M = Sc, Ti, V, Cr, Mn, Fe, Y, Zr, Nb, Mo, Hf, Ta) using the self consistent tight-binding linear muffin-tin orbital method. The equilibrium volume, bulk moduli, pressure derivative of bulk moduli, cohesive energy, heat of formation, and electronic specific heat coefficient were calculated for these systems and compared with the available experimental and other theoretical results. The bonding nature of these diborides was analyzed via the density of states histogram as well as the charge density plots, and the chemical stability was analyzed using the band filling principle. The variation in the calculated cohesive properties of these materials was correlated with the band filling effect. The existence of a pseudogap in the total density of states was found to be a common feature for all these compounds. The reason for the creation of the pseudogap was found to be due to the strong covalent interaction between boron *p* states. Fedor-

chenko and Grechnev with coauthors [13,14] measured the temperature dependences of the magnetic susceptibility χ and its anisotropy $\Delta\chi = \chi_{\|} - \chi_{\perp}$ for single crystals of transition-metal diborides MB_2 (M = Sc, Ti, V, Zr, Hf) in the temperature interval 4.2–300 K. A transition into the superconducting state was not found in any of the diborides studied, right down to liquid-helium temperature. It was found that the anisotropy is weakly temperature-dependent, a nonmonotonic function of the filling of the hybridized *p–d* conduction band. First-principles calculations of the electronic structure of diborides and the values of the paramagnetic contributions spin and Van Vleck to their susceptibility show that the behavior of the magnetic anisotropy is due to the competition between Van Vleck paramagnetism and orbital diamagnetism of the conduction electrons. Duan *et al*. [23] calculated elastic constants of 24 compounds of the AlB_2-type diborides including ScB_2 by first-principles with the generalized gradient approximation using the Voigt–Reuss–Hill averaging scheme. Values of all independent elastic constants as well as bulk modulus in *a* and *c* directions were predicted. It was founded that AlB_2 is more ductile while ScB_2 is more brittle, and AlB_2 has a highest elastic anisotropy in the 24 AlB_2-type compounds. Deligoz *et al*. [15] investigated the structural and lattice dynamical properties of MB_2 (M = Sc, V, Ti) using first-principles total energy calculations. Specifically, the lattice parameters (*a*, *c*) of the stable phase, the bond lengths of M–B and B–B atoms, phonon dispersion curves and the corresponding density of states, and some thermodynamical quantities such as internal energy, entropy, heat capacity, and their temperature-dependent behaviors, were presented. The obtained results for structural parameters are in a good agreement with the available experimental data. Zhang *et al*. [19] presented extensive structure searches to uncover the high-pressure structures of MB_2 (M = Sc, Ti, Y, and Zr) up to 300 GPa using the *ab initio* evolutionary algorithm [24]. They show that ZrB_2 persists up to 300 GPa within an ambient-pressure AlB_2-type structure, while pressure-induced transitions into monoclinic phases (*C*2/*m*, *Z* = 4) occur for ScB_2 at 208 GPa and YB_2 at 163 GPa. A tetragonal R-$ThSi_2$ structure (*I*41/*amd*, *Z* = 4) for TiB_2 at 215 GPa was predicted. The phase transformation mechanism has been discussed.

The properties of the Fermi surface of ScB_2, ZrB_2, and HfB_2 single crystals were studied by Pluzhnikov *et al*. [25] using the de Haas–van Alphen effect. The angular dependences of the frequencies of the dHvA oscillations in the planes $(10\bar{1}0)$, $(11\bar{2}0)$, and (0001) and the values of their effective cyclotron masses were measured. The frequencies of the oscillations in ScB_2 found lie in the interval $(2.09–23.6)\cdot10^2$ T and the measured cyclotron masses lie in the range $(0.26–0.87)m_0$.

Despite a lot of publications, there are still many open questions related to the electronic structure and physical properties of ScB_2 diboride. The theoretical efforts were devoted mostly to the lattice and mechanical properties of ScB_2. There is no theoretical explanation of the Fermi surface as well as angle dependence of the cyclotron masses and extremal cross sections of the Fermi surface, electron–phonon interaction and electrical resistivity in ScB_2. The aim of this work is a complex investigation of the electronic structure, Fermi surface, angle dependence of the cyclotron masses and extremal cross sections of the Fermi surface, phonon spectra, electron–phonon Eliashberg and transport spectral functions, and temperature dependence of electrical resistivity of the ScB_2 diboride.

The paper is organized as follows. Section 2 presents the details of the calculations. Section 3 is devoted to the electronic structure as well as the Fermi surface, angle dependence of the cyclotron masses and extremal cross sections of the Fermi surface, phonon spectra, electron–phonon interaction and electrical resistivity using the fully relativistic and full potential LMTO band structure methods. The results are compared with available experimental data. Finally, the results are summarized in Sec. 4.

2. Computational details

Most known transition-metal (M) diborides MB_2 are formed by group III–VI transition elements (Sc, Ti, Zr, Hf, V, Nb, and others) and have a layered hexagonal *C*32 structure of the AlB_2-type with the space group symmetry *P*6/*mmm* (number 191). It is simply a hexagonal lattice in which closely-packed transition metal layers alternating with graphite-like B layers (Fig. 1). These diborides cannot be exactly layered compounds because the interlayer interaction is strong even though the M layers alternate with the B layers in their crystal structure. The boron atoms lie on the corners of hexagons with the three nearest neighbor boron atoms in each plane. The M atoms lie directly in the centers of each boron hexagon, but midway between adjacent boron layers. Each transition metal atom has 12 nearest neighbor B atoms and eight nearest neighbor transition metal atoms (six are on the metal plane and two out of the metal plane). There is one formula unit per primitive cell and the crystal has simple hexagonal symmetry (*D*6*h*). By choosing

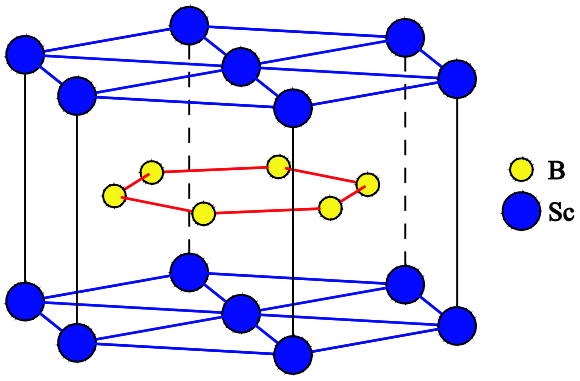

Fig. 1. (Color online) Schematic representation of the ScB_2 crystal structure.

appropriate primitive lattice vectors, the atoms are positioned at Sc (0,0,0), B (1/3,1/6,1/2), and B (2/3,1/3,1/2) in the unit cell. The distance between Sc–Sc is equal to *c*. This structure is quite close packed, and can be coped with efficiently and accurately by the atomic sphere approximation method. However, for precise calculation of the phonon spectra and electron–phonon interaction, a full potential approximation should be used.

The Eliashberg function (the spectral function of the electron–phonon interaction) expressed in terms of the phonon linewidths $\gamma_{\mathbf{q}\nu}$ has the form [26]

$$\alpha^2 F(\omega) = \frac{1}{2\pi N(\varepsilon_F)} \sum_{\mathbf{q}\nu} \frac{\gamma_{\mathbf{q}\nu}}{\omega_{\mathbf{q}\nu}} \delta(\omega - \omega_{\mathbf{q}\nu}). \quad (1)$$

The line-widths characterize the partial contribution of each phonon:

$$\gamma_{\mathbf{q}\nu} = 2\pi\omega_{\mathbf{q}\nu} \sum_{jj'\mathbf{k}} |\, g^{\mathbf{q}\nu}_{\mathbf{k}+\mathbf{q}j',\mathbf{k}j} \,|^2 \, \delta(\varepsilon_{j\mathbf{k}} - \varepsilon_F)\delta(\varepsilon_{\mathbf{k}+\mathbf{q}j'} - \varepsilon_F). \quad (2)$$

The electron–phonon interaction constant is defined as

$$\lambda_{e-\mathrm{ph}} = 2\int_0^\infty \frac{d\omega}{\omega} \alpha^2 F(\omega). \quad (3)$$

It can also be expressed in terms of the phonons linewidths:

$$\lambda_{e-\mathrm{ph}} = \sum_{\mathbf{q}\nu} \frac{\gamma_{\mathbf{q}\nu}}{\pi N(\varepsilon_F)\omega^2_{\mathbf{q}\nu}}, \quad (4)$$

were $N(\varepsilon_F)$ is the electron density of states per atom and per spin on the Fermi level and $g^{q\nu}_{\mathbf{k}+qj'\mathbf{k}j}$ is the electron–phonon interaction matrix element. The double summation over Fermi surface in Eq. (2) was carried out on dense mesh (793 point in the irreducible part of the Brilloin zone (BZ)).

Calculations of the electronic structure and physical properties of the ScB_2 diborides were performed using fully relativistic LMTO method [27] with the experimentally observed lattice constants: a = 3.117 Å and c = 3.407 Å [15]. For the calculation of the phonon spectra and electron–phonon interaction a scalar relativistic FP-LMTO method [28] was used. In our calculations we used the Perdew–Wang [29] parameterization of the exchange-correlation potential in general gradient approximation. BZ integrations were performed using the improved tetrahedron method [30]. Phonon spectra and electron–phonon matrix elements were calculated for 50 points in the irreducible part of the BZ using the linear response scheme developed by Savrasov [28]. The 3*s* and 3*p* semi-core states of ScB_2 were treated as valence states in separate energy windows. Variations in charge density and potential were expanded in spherical harmonics inside the MT sphere as well as 2894 plane waves in the interstitial area with 88.57 Ry cut-off energy. As for the area inside the MT spheres, we used 3*k*–*spd* LMTO basis set energy (–0.1, –1, –2.5 Ry) with one-center expansions inside the MT-spheres performed up to $l_{\max}$ = 6.

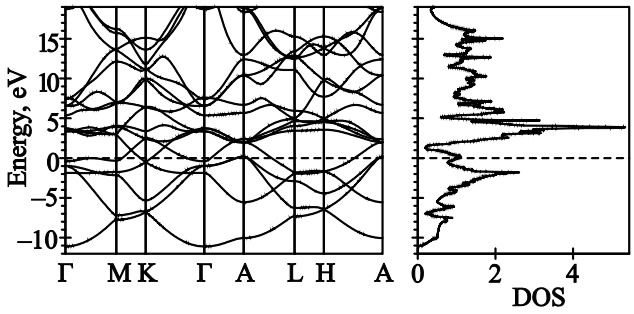

Fig. 2. (Color online) Energy band structure and total DOS [in states/(cell·eV)] of ScB_2.

3. Results and discussion

3.1. Energy band structure

Figure 2 presents the energy band structure and total density of states of ScB_2. The partial DOSs ScB_2 are shown in Fig. 3. Our results for the electronic structure of ScB_2 are in a good agreement with earlier calculations [9,11,13,14,23]. The Sc 3*d* states are the dominant features in the interval from -10.0 to 12 eV. These tightly bound states show overlap with B 2*p* and, to a lesser extent, with B 2*s* states both above and below ε_F, implying consider-

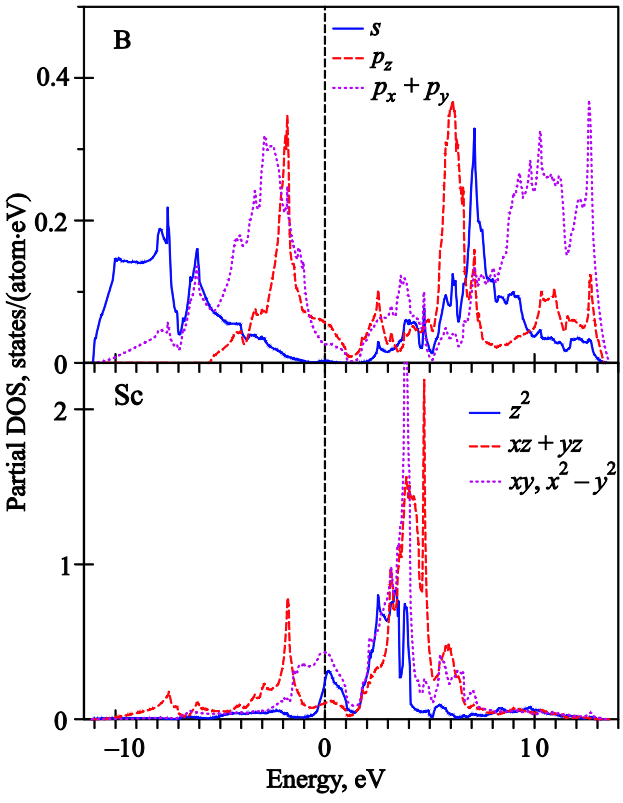

Fig. 3. (Color online) Partial density of states of ScB_2.

able covalency. The crystal field at the Sc site (*D*6*h* point symmetry) causes the splitting of Sc *d* orbitals into a singlet $a_{1g}(d_{3z^2-1})$ and two doublets e_{1g} (d_{yz} and d_{xz}) and e_{2g} (d_{xy} and $d_{x^2-y^2}$). The crystal field at the B site (*D*3*h* point symmetry) causes the splitting of B *p* orbitals into a singlet $a_4(p_z)$ and a doublet e_2 (p_x and p_y). B *s* states occupy a bottom of valence band between -11.1 eV and -1.0 eV and hybridize strongly with B p_x and p_y and Sc d_{xz} and d_{yz} states. B p_x and p_y occupied states are located between -11.0 eV and ε_F. B p_z states occupied a smaller energy interval from -5.5 eV to ε_F with a very strong and narrow peak structure at around -2 eV. ScB_2 diboride has partially unoccupied bonding bands. The Sc *d* band along $\Gamma - M$ is below ε_F (Fig. 2) and the large contribution to $N(\varepsilon_F)$ is due to Sc *d* states. There is a small hole concentration of B $2p_{x,y}$ states at *A* symmetry point. Thus, one can expect for ScB_2 only low-temperature superconductivity.

3.2. Fermi surface

The Fermi surface (FS) of ScB_2 consists of three sheets: two small almost identical closed hole ellipsoids around A symmetry point (Fig. 4(a)) and open large electron sheet derived from the crossing of the Fermi energy by the 5th energy band (Fig. 4(b)). Figure 5 shows the calculated Fermi surface cross section areas of ScB_2 in the plane perpendicular to the z direction and crossed A symmetry point, crossed Γ point and in the plane at half distance between A and Γ points.

The Fermi surfaces of ScB_2, ZrB_2, and HfB_2 were studied by Pluzhnikov *et al*. [25] using the dHvA effect. Figure 6 represents angular variations of the experimentally measured dHvA frequencies [25] for ScB_2 in comparison with the first-principle calculations for field direction in

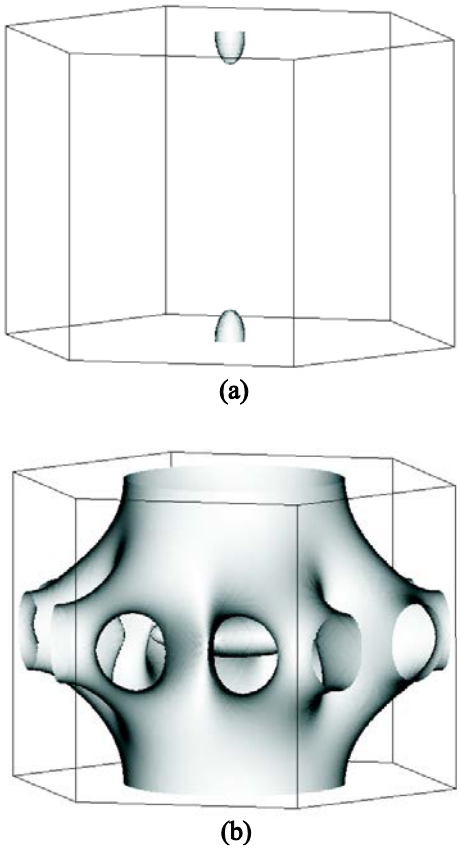

Fig. 4. (Color online) The calculated hole sheet of the Fermi surface around A symmetry point from the 3rd energy band (a) and electron sheet from the 5th energy band (b) in ScB_2.

the $(10\bar{1}0)$, $(11\bar{2}0)$, and (0001) planes. The observed dependences τ, φ, and Ψ show that these fragments of the FS are strongly anisotropic, and the dependences of π and σ are close to an ellipsoidal frequencies. The theoretical calculations reveal that π and σ oscillations indeed belong to hole ellipsoids around the *A* symmetry point. The φ, τ, and Ψ orbits belong to large open electron FS. Two

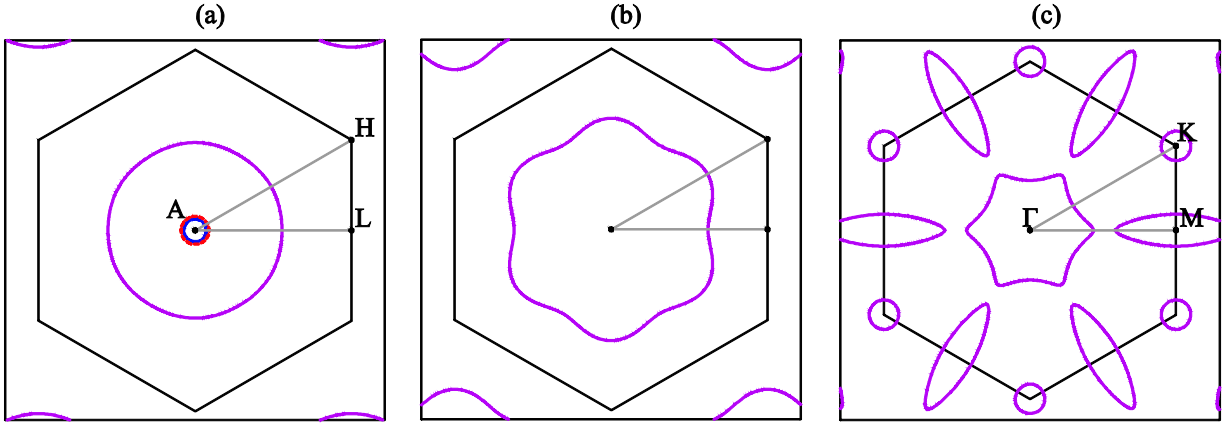

Fig. 5. (Color online) The calculated Fermi surface cross section areas of ScB_2 in the plane perpendicular to the z direction and cross A symmetry point (a), cross Γ point (c) and in the plane at half distance between A and Γ points (b). The cross sections of hole ellipsoids present by full blue curve and red dashed curve for the 3rd and 4th energy bands, respectively. The magenta curves at all three panels show the cross sections of the Fermi surface for the electron sheet corresponding to the 5th energy band.

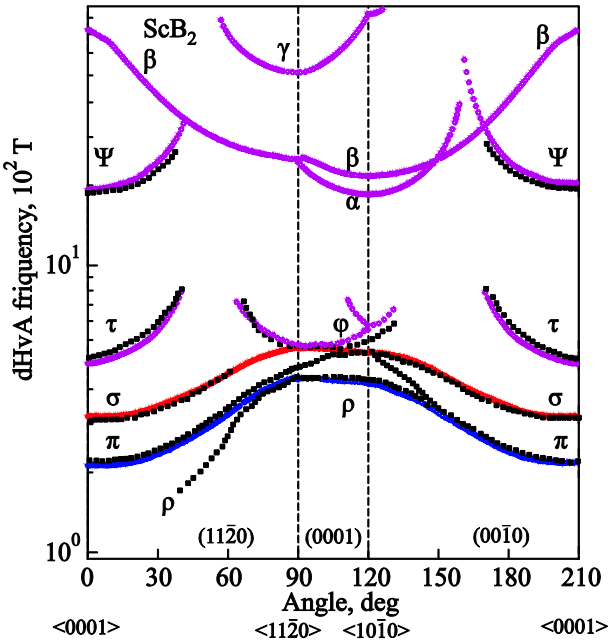

Fig. 6. (Color online) The calculated (open red, blue and magenta circles) and experimentally measured [25] (black full squares) angular dependence of the dHvA oscillation frequencies in the compound ScB_2.

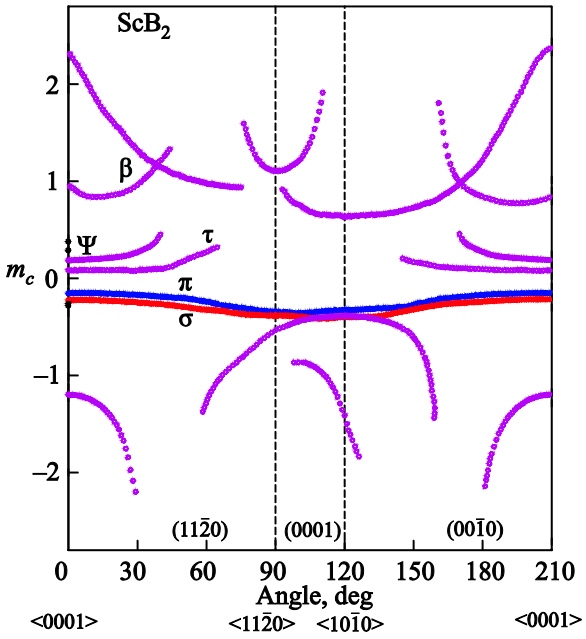

Fig. 7. (Color online) The calculated angular dependence of the cyclotron masses in ScB_2 (open red, blue and magenta circles) and experimentally measured ones [25] (black full squares).

hole ellipsoids around A point have almost identical form and slightly different size, as a result they have similar Fermi surface cross section areas (π and σ orbits for the 3rd and 4th energy bands, respectively) appeared at all the three planes (Fig. 6). The theory reasonably well reproduces the experimentally measured frequencies for the σ, φ, τ, and Ψ orbits. However, at the (11$\bar{2}$0) plane we were not able to detect low frequency β orbit observed experimentally. The experiment for high frequencies detected only Ψ orbits in vicinity of the $<0001>$ direction in ScB_2. We found an additional α, β and γ orbits situated at the electron FS. These orbits have not been detected in the dHvA experiment [25]. One of the possible reasons for that is the relatively large cyclotron masses for these orbits. Figure 7 shows the theoretically calculated angular dependence of the cyclotron masses (m_b) and the experimentally measured masses (m_c^*) in ScB_2. The cyclotron effective masses were determined from the temperature dependences of the amplitudes of the dHvA oscillations. The cyclotron masses for the α, β and γ orbits are much larger than for the corresponding low-frequency oscillations π, σ, τ, and Ψ.

We note that band cyclotron effective masses m_b are renormalized by the electron–phonon interaction $m_c^* = m_b(1+\lambda)$, where λ is the constant of the electron–phonon interaction. By comparing the experimentally measured cyclotron masses with band masses we can estimate the λ. It is strongly varied on the orbit type and magnetic direction. We estimate the constant of the electron–phonon interaction to be equal to 0.16 and 0.41 for the π and σ hole orbits, respectively, with **H** || <0001>. The constant λ for the electron orbits is significantly larger and equal to 0.9 and 1.1 for the Ψ and τ orbits, respectively.

3.3. Phonon spectra

The unit cell of ScB_2 contains three atoms, which gives in general case a nine phonon branches. Figure 8 shows theoretically calculated phonon dispersion curves along Γ–A symmetry direction in ScB_2. Figure 9 shows theoretically calculated phonon density of state for ScB_2 (full blue curve). The DOS for ScB_2 can be separated into three distinct regions. Based on our analysis of relative directions of eigenvectors for each atom in unit cell, we found that the first region (with a peak in phonon DOS at 26.9 meV) is dominated by the motion of Sc. This region belongs

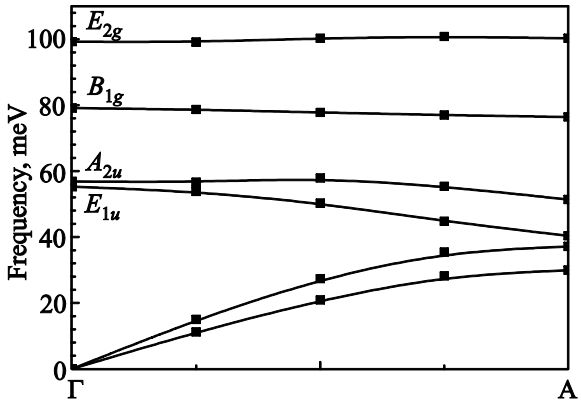

Fig. 8. (Color online) Theoretically calculated phonon dispersion curves along Γ–A symmetry direction in ScB_2.

to the acoustic phonon modes. The second wide region (54–83 meV) results from the coupled motion of Sc and the two B atoms in the unit cell. The E_{1u}, A_{2g}, B_{1g} phonon modes lie in this area (see Fig. 8 and Table 1). The phonon DOS in the third region extends from 83 to 100 meV. This is due to the movement of boron atoms and is expected since boron is lighter than Sc. The covalent character of the B–B bonding is also crucial for the high frequency of phonons. The in-plane E_{2g} mode belongs to this region. The second and third regions represent optical phonon modes in crystals. The most significant feature in the phonon DOS is a gap around 33–54 meV. This gap is a consequence of the large mass difference between B and Sc, which leads to decoupling of the transition metal and boron vibrations.

Table 1. Theoretically calculated phonon frequencies (in meV) in the Γ symmetry point for ScB_2 and calculated ones by Deligoz *et al.* [15]

Reference	E_{1u}	A_{2g}	B_{1g}	E_{2g}
Our results	55.247	56.85	79.113	99.29
Ref. 15	55.72	56.11	77.08	99.72

Currently, there are no data concerning the experimentally measured phonon DOS in ScB_2. So we compare our results with theoretically calculated phonon DOS by Deligoz *et al.* [15] (Fig. 9). Calculations of these authors were based on the density functional formalism and generalized gradient approximation. They used the Perdew–Burke–Ernzerhof functional [31] for the exchange-correlation energy as it is implemented in the SIESTA code [32]. This code calculates the total energies and atomic Hellmann–Feynman forces using a linear combination of atomic orbitals as the basis set. The basis set consists of finite range pseudoatomic orbitals of the Sankey–Niklewsky type [33] was generalized to include multiplezeta decays. The interactions between electrons and core ions were simulated with the separable Troullier–Martins [34] normconserving pseudopotentials. In other words, they used the so-called "frozen phonon" technique and built an optimized rhombohedral supercell with 36 atoms. This method is inconvenient for calculating phonon spectra for small **q** points as well as for compounds with large number of atoms per unit cell.

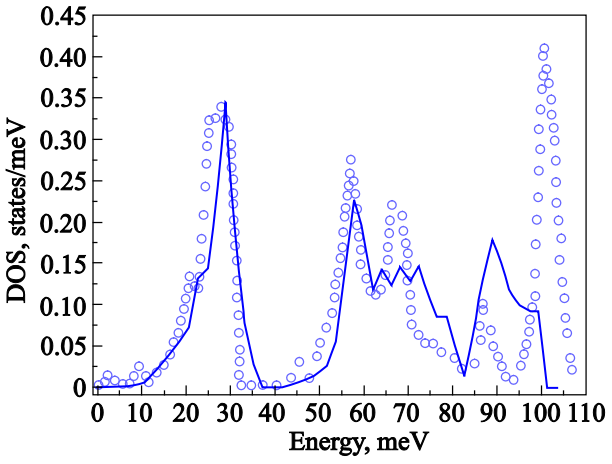

Fig. 9. (Color online) Theoretically calculated phonon density of states (full blue line) for ScB_2. The open circles presents the calculated phonon DOS of ScB_2 by Deligoz *et al.* [15].

There is a good agreement between our calculations and the results of Deligoz *et al.* [15] in a shape and energy position of the first peak in the phonon DOS. The second and third regions consist of two peak each, in both the regions high-energy peaks have smaller intensity in our calculations in comparison with results of Deligoz *et al.* [15] (see also Table 1). There is also small high-energy shift of the third peak in Deligoz *et al.* [15] in comparison with our results.

3.4. Electron–phonon interaction

Figure 10(a) shows theoretically calculated Eliashberg functions for ScB_2. There are two main differences in comparison with phonon DOS curve. Low-energy peak is significantly reduced and shifted downwards by 1.6 meV. Wide 62–83 meV shoulder transform into two peaks on 68.3 and 72.8 meV. Analysis of electron–phonon prefactor $\alpha^2(\omega)$ ($\alpha^2(\omega) \equiv \alpha^2(\omega)F(\omega)/F(\omega)$) shows that B_{2g} phonon mode has strong coupling with electronic subsystem and significantly expands middle-energy region on Eliashberg curve. As consequence, averaged electron–phonon interaction constant $\lambda_{e-\mathrm{ph}}$ is reasonably large and equal to 0.47.

A unique feature of electron–phonon coupling in MgB_2 (T_c = 39 K) is the down-shift of the in-plane E_{2g} mode well below the out-of-plane B_{1g} mode [35]. Such an inversion of the usual sequence of mode frequencies give one wide continuous peak formed from medium- and high-energy regions. ScB_2 to some extend is situated in the middle between MB_2 (M = Ti, Zr, and Hf) and MgB_2 diborides. Superconductivity in MgB_2 is also related to the existence of B $2p_{x,y}$ band hole along the Γ–A direction. Moreover, according to Ref. 36, the existence of degenerate $p_{x,y}$ states above ε_F in the Brillouin zone is crucial

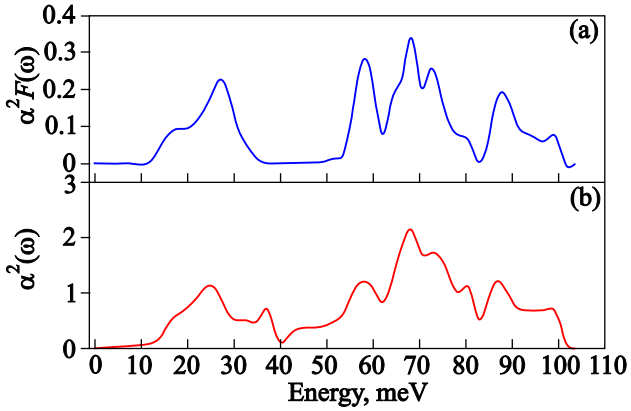

Fig. 10. (Color online) Theoretically calculated Eliashberg function $\alpha^2F(\omega)$ of ScB_2 (a) and electron–phonon prefactor $\alpha^2(\omega)$ (b).

for the supercondactivity in diborides. The $2D{-}2p_{x,y}$ bands in ScB_2 are partially filled with small hole concentration near *A* point (see Figs. 2 and 3). On the other hand, the Fermi level for MB_2 (M = Ti, Zr, and Hf) diborides falls in the pseudogap and the B $2p_{x,y}$ bands are completely filled [14,35,37]. A systematic experimental search in the past for superconductivity in the *d* diborides showed that T_c for MB_2 (M = Ti, Zr, Hf, V, Nb, Cr, Mo, U) is below 0.4 K [2].

To calculate the T_c for ScB_2, we used in our calculations McMillan formula modified by Allen–Dynes [38]:

$$T_c = \frac{\omega_{\log}}{1.2}\left(-\frac{1.04(1+\lambda)}{\lambda-\mu^*(1+0.62\lambda)}\right), \qquad (5)$$

where $\omega_{\log}$ is the effective logarithmically averaged phonon frequency, μ^* is the screening Coulomb pseudopotential. We obtained T_c =1.62 K (μ^* = 0.14) in good agreement with the experimental value 1.5 K [5]. Relatively low value can be explained by smallest $\omega_{\log}$ among all transition metal diborides (see Table 2). This quantity represents the effective average frequency of the coupling modes and sets the energy scale for the pairing interaction. Its small value indicates that the pairing interaction is mainly mediated by the *d* atom vibrations and not by the boron modes.

Table 2. The values of $\lambda_{e-\mathrm{ph}}$ and $\omega_{\log}$ for transition metal diborides

Diborides	ScB_2	ZrB_2 [39]	TiB_2 [39]	HfB_2 [40]
$\lambda_{e-\mathrm{ph}}$	0.47	0.14	0.15	0.17
$\omega_{\log}$	372.23	520.37	582.13	459.25

3.5. Electrical resistivity

In the pure metals (excluding low-temperature region), the electron–phonon interaction is the dominant factor governing electrical conductivity of the substance. Using lowest-order variational approximation, the solution for the Boltzmann equation gives the following formula for the temperature dependence of $\rho_I(T)$:

$$\rho_I(T) = \frac{\pi\Omega_{\mathrm{cell}}k_BT}{N(\varepsilon_F)\langle v_I^2\rangle}\int_0^\infty \frac{d\omega}{\omega}\frac{\xi^2}{\sinh^2\xi}\alpha_{\mathrm{tr}}^2F(\omega), \qquad (6)$$

where the subscript I specifies the direction of the electrical current. In our work, we investigate two direction: [0001] (*c* axis or z direction) and $[10\bar{1}0]$ (*a* axis or *x* direction). $\langle v_I^2\rangle$ is the average square of the I component of the Fermi velocity, $\xi = \omega/2k_BT$.

Mathematically, the transport function $\alpha_{\mathrm{tr}}F(\omega)$ differs from $\alpha F(\omega)$ only by an additional factor $[1-v_I(\mathbf{k})v_I(\mathbf{k}')/\langle v_I^2\rangle]$, which preferentially weights the backscattering processes.

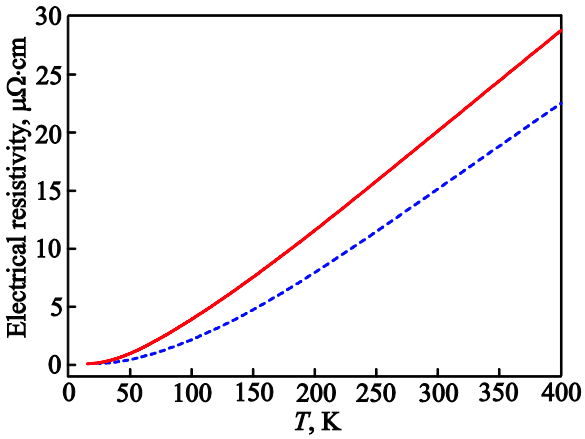

Fig. 11. (Color online) Temperature dependence of electrical resistivity in ScB_2. Theoretically calculated for the <0001> direction (dashed blue curve) and the basal $<10\bar{1}0>$ direction (full red curve).

Formula (6) remains valid in the range $\Theta_{\mathrm{tr}}/5 < T < 2\Theta_{\mathrm{tr}}$ [28], where

$$\Theta_{\mathrm{tr}} \equiv \langle\omega^2\rangle_{\mathrm{tr}}^{1/2}, \qquad (7)$$

$$\langle\omega^2\rangle_{\mathrm{tr}} = \frac{2}{\lambda_{\mathrm{tr}}}\int_0^\infty \omega\alpha_{\mathrm{tr}}^2F(\omega)d\omega, \qquad (8)$$

$$\lambda_{\mathrm{tr}} = 2\int_0^\infty \alpha_{\mathrm{tr}}^2F(\omega)\frac{d\omega}{\omega}. \qquad (9)$$

The low-temperature electrical resistivity is the result of electron–electron interaction, size effects, scattering on impurities, etc., however, for high temperatures it is necessarily to take into account the effects of anharmonicity and the temperature smearing of the Fermi surface. In our calculations Θ_{tr} = 606.69 K for *c* axis, and 500.7 for *a* axis for ScB_2.

Figure 11 represents the theoretically calculated temperature dependence of electrical resistivity in ScB_2. We obtained anisotropy ratio of electrical resistivity at T = = 300 K: ρ_x/ρ_z = 1.33. Among previously studied diborides (HfB_2, ZrB_2 and TiB_2) [39,40] ScB_2 has the highest degree of anisotropy.

4. Summary

We have studied the electronic structure and physical properties of ScB_2 using fully relativistic and full potential linear muffin-tin orbital methods. We study the electron and phonon subsystems as well as the electron–phonon interaction in this compound.

We investigated the Fermi surface, angle dependence of the cyclotron masses, and extremal cross sections of the Fermi surface of ScB_2 in details. Theoretical calculations show that the Fermi surface of ScB_2 consists of three sheets: two small almost identical closed hole ellipsoids

around A symmetry point and open large electron sheet derived from the crossing of the Fermi energy by the 5th energy band. The angle variation of the τ, φ, and Ψ show that these fragments of the FS are strongly anisotropic, and the dependencies of π and σ are close to an ellipsoidal frequencies. The theoretical calculations reveal that π and σ oscillations belong to hole ellipsoids around the A symmetry point. The φ, τ, and Ψ orbits belong to large open electron FS. Two hole ellipsoids around A point have almost identical form and slightly different size, as a result they have similar Fermi surface cross section areas. The theory reproduces the experimentally measured frequencies for the σ, φ, τ, and Ψ orbits reasonably well. However, at the $(11\bar{2}0)$ plane we were not able to detect low frequency β orbit observed experimentally. The experiment for high frequencies detected only Ψ orbits in vicinity of the <0001> direction in ScB_2. We found an additional α, β and γ orbits situated at the electron FS. These orbits have not been detected in the dHvA experiment [25]. One of the possible reasons for that is the relatively large cyclotron masses for these orbits. We found that the cyclotron masses for the α, β and γ orbits are much larger than for the corresponding low-frequency oscillations π, σ, τ, and Ψ.

Calculated phonon spectra and phonon DOSs for ScB_2 is in good agreement with previous calculations. The averaged electron–phonon interaction constant was found to be rather large $\lambda_{e-\mathrm{ph}} = 0.47$ for ScB_2. We calculated the temperature dependence of the electrical resistivity for ScB_2 in the lowest-order variational approximation of the Boltzmann equation. We obtained rather large anisotropy ratio of electrical resistivity at $T = 300$ K: $\rho_x/\rho_z = 1.33$.

Acknowledgments

This work was carried out at the Ames Laboratory, which is operated for the U.S. Department of Energy by Iowa State University under Contract No. DE-AC02-07CH11358. This work was supported by the Director for Energy Research, Office of Basic Energy Sciences of the U.S. Department of Energy. V.N.A. gratefully acknowledges the hospitality during his stay at Ames Laboratory.

This work was also supported by the National Academy of Sciences of Ukraine in the framework of the State Target Scientific and Technology Program "Nanotechnology and Nanomaterials" for 2010–2014 (No. 0277092303) and Implementation and Application of Grid Technologies for 2009-2013 (No. 0274092303).

1. J. Nagamatsu, N. Nakagawa, T. Muranaka, Y. Zenitani, and J. Akimitsu, *Nature* (*London*) **410**, 63 (2001).
2. V.A. Gasparov, N.S. Sidorov, I.I. Zverkova, and M.P. Kulakov, *JETP Lett*. **73**, 532 (2001).
3. D.P. Young, R.G. Goodrich, P.W. Adams, J.Y. Chan, F. R. Fronczek, F. Drymiotis, and L.L. Henry, *Phys. Rev. B* **65**, 180518 (2002).
4. C. Buzea and T. Yamashita, *Supercond. Sci. Technol*. **14**, R115 (2001).
5. G.V. Samsonov and I.M. Vinitsky, *Refractory Compounds*, Metallurgija, Moskva (1976) (in Russian).
6. J.K. Burdett, E. Canadell, and G.J. Miller, *J. Am. Chem. Soc.* **108**, 6561 (1986).
7. A.F. Guillerment and G. Grimvall, *J. Less-Common Met*. **169**, 257 (1991).
8. B. Wang, D.C. Tian, and L.L. Wang, *J. Phys.: Condens. Matter* **6**, 10185 (1994).
9. A.L. Ivanovskii, N.I. Medvedeva, and J.E. Medvedeva, *Metallofiz. Noveishie Tekhnol*. **21**, 19 (1999).
10. N.I. Medvedeva, A.L. Ivanovskii, J.E. Medvedeva, and A.J. Freeman, *Phys. Rev. B* **64**, 020502 (2001).
11. P. Vajeeston, P. Ravindran, C. Ravi1, and R. Asokamani, *Phys. Rev. B* **63**, 045115 (2001).
12. X. Zhang, X. Luo, J. Han, J. Li, and W. Han, *Comput. Mat. Sci*. **44**, 411 (2008).
13. G.E. Grechnev, A.V. Fedorchenko, A.V. Logosha, A.S. Panfilov, I.V. Svechkarev, V.B. Filippov, A.B. Lyashchenko, and A.V. Evdokimova, *J. Alloys Comp*. **481**, 75 (2009).
14. A.V. Fedorchenko, G.E. Grechnev, A.S. Panfilov, A.V. Logosha, I.V. Svechkarev, V.B. Filippov, A.B. Lyashchenko, and A.V. Evdokimova, *Fiz. Nizk. Temp*. **35**, 1106 (2009) [*Low Temp. Phys*. **35**, 862 (2009)].
15. E. Deligoz, K. Colakoglu, and Y. Ciftci, *Solid State Commun*. **149**, 1843 (2009).
16. J.-D. Zhang and X.-L.Cheng, *Physica B* **405**, 3532 (2010).
17. X. Zhang, X. Luo, J. Li, P. Hu, and J. Han, *Scripta Materialia* **62**, 625 (2010).
18. E. Deligoz, K. Colakoglu, and Y.O. Ciftci, *Comp. Mat. Sci.* **47**, 875 (2010).
19. M. Zhang, H. Wang, H. Wang, X. Zhang, T. Iitaka, and Y. Ma, *Inorg. Chem*. **49**, 6859 (2010).
20. J.-D. Zhang, X.-L. Cheng, and D.-H. Li, *J. Alloys Comp*. **509**, 9577 (2011).
21. H. Li, L. Zhang, Q. Zeng, and L. Cheng, *J. Phase Equilibria & Diffusion* **32**, 422 (2011).
22. J.W. Lawson, C.W. Bauschlicher, and M.S. Daw, *J. American Ceramic Society* **94**, 3494 (2011).
23. Y.H. Duan, Y. Sun, Z.Z. Guo, M.J. Pang, P.X. Zhu, and J.H. He, *Comp. Mat. Sci*. **51**, 112 (2012).
24. A.R. Oganov and C.W. Glass, *J. Chem. Phys*. **124**, 244704 (2006).
25. V.B. Pluzhnikov, I.V. Svechkarev, A.V. Dukhnenko, A.V. Levchenko, V.B. Filippov, and A. Chopnik, *Fiz. Nizk. Temp*. **33**, 473 (2007) [*Low Temp. Phys*. **33**, 350 (2007)].
26. P.B. Allen, *Phys. Rev. B* **6**, 2577 (1972).
27. V.N. Antonov, A.Y. Perlov, A.P. Shpak, and A.N. Yaresko, *J. Magn. Magn. Mater*. **146**, 205 (1995).
28. S.Y. Savrasov and D.Y. Savrasov, *Phys. Rev. B* **54**, 16470 (1996).
29. J. Perdew and Y. Wang, *Phys. Rev. B* **45**, 13244 (1992).
30. P.E. Blöchl, O. Jepsen, and O.K. Andersen, *Phys. Rev. B* **49**, 16223 (1994).

31. J.P. Perdew, K. Burke, and M. Ernzerhof, *Phys. Rev. Lett*. **77**, 3865 (1996).
32. P. Ordejon, E. Artacho, and J.M. Soler, *Phys. Rev. B* **53**, R10441 (1996).
33. O.F. Sankey and D.J. Niklewski, *Phys. Rev. B* **40**, 3979 (1989).
34. J.M.N. Troullier, *Phys. Rev. B* **43**, 1993 (1991).
35. H. Rosner, J.M. An, W.E. Pickett, and S.-L. Drechsler, *Phys. Rev. B* **66**, 024521 (2002).
36. J. Nagamatsu, *Nature* **63**, 410 (2001).
37. Y.G. Naidyuk, O.E. Kvitnitskaya, I.K. Yanson, S.-L. Drechsler, G. Behr, and S. Otani, *Phys. Rev. B* **66**, 140301(R) (2002).
38. P.B. Allen and R.C. Dynes, *Phys. Rev. B* **12**, 905 (1975).
39. S.M. Sichkar, V.N. Antonov, and V.P. Antropov, *Phys. Rev. B* **87**, 064305 (2013).
40. S.M. Sichkar and V.N. Antonov, *preprint cond-mat/0650138* (2013).